

PARTICLE-IN-CELL SIMULATIONS OF NON-LOCAL
EFFECTS IN INDUCTIVELY COUPLED PLASMAS

A Comprehensive Report Submitted to the
Department of Physics and Engineering Physics
in Partial Fulfillment of the Requirements
for the degree of Master of Science
at the University of Saskatchewan
Saskatoon, Saskatchewan S7N 5A9

By

Aaron Froese

©Aaron Froese, September 2006. All rights reserved.

ABSTRACT

Utilizing a particle-in-cell (PIC) code, an inductively coupled plasma (ICP) with finite temperature was studied to determine plasma properties such as the ponderomotive force (PMF) and the surface impedance. In the low pressure, low frequency regime, electron mean free paths are large relative to device size and the trajectories are strongly influenced by the induced rf magnetic field. This causes problems for classical, local theories, which are unable to integrate the effects accumulated along each nonlinear path, especially considering the initial thermal distribution of the particles.

If the nonlinearities are ignored, the simulated PMF is proportional to the amplitude of the driving electromagnetic wave squared, in agreement with analytic theories. When the full dynamics is simulated, the exponent changes from a simple square to include a term that scales with the logarithm of the temperature. This implies there is a critical temperature where the transit time of a thermal electron through the skin is comparable to the driving period, below which all plasmas can be assumed to be cold.

Again ignoring nonlinearities, the calculated surface impedance agrees with collisionless theoretical values very well. The plasma is highly reflective at low frequencies, but slowly becomes absorptive near the resonant Landau frequency. With full dynamics, however, the transition between the reflective and absorptive regimes occurs much more quickly. The frequency of peak absorption also increases as the amplitude of the driving wave is increased, contrary to linear results.

CHAPTER 1

INDUCTIVELY COUPLED PLASMAS

1.1 Overview

An inductively coupled plasma (ICP) is formed when an electromagnetic (EM) wave travels through a low density gas. This is usually accomplished by winding a coil around a vacuum chamber to form a solenoid or forming a stove-top element shape and placing it at the end of the cylinder. A radio frequency (rf) alternating current is excited in the coil, which creates an EM wave that propagates through the cylinder, ionizing the gas and creating a plasma.

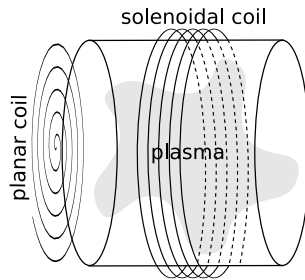


Figure 1.1: ICP antenna configurations can be solenoidal or planar. Both induce an azimuthal electric field.

ICP devices are commonly used for microscale etching, spectroscopy, and low-maintenance lighting. The plasma is usually of a higher density in semiconductor processing to produce a high etch rate, while the same is true for spectrochemical analysis to rapidly ionize the sample. It can be maintained without contacting the chamber walls, which would otherwise contaminate the sample, and also increases the longevity of the device. All applications benefit from the low power input requirements required to drive the rf coil.

Once the plasma forms, it inhibits the propagation of the radiation. The EM wave becomes evanescent upon entry into the plasma, creating a skin layer which essentially acts as a counter-winding to the coil. The wave is reflected, heating the plasma and imparting a force to it. Three quantities determine the interaction regime of a wave with a plasma: the driving frequency ω , the collision frequency ν , and the thermal frequency kv_{Te} , or rate at which a thermal electron traverses the skin layer. If the driving frequency is high

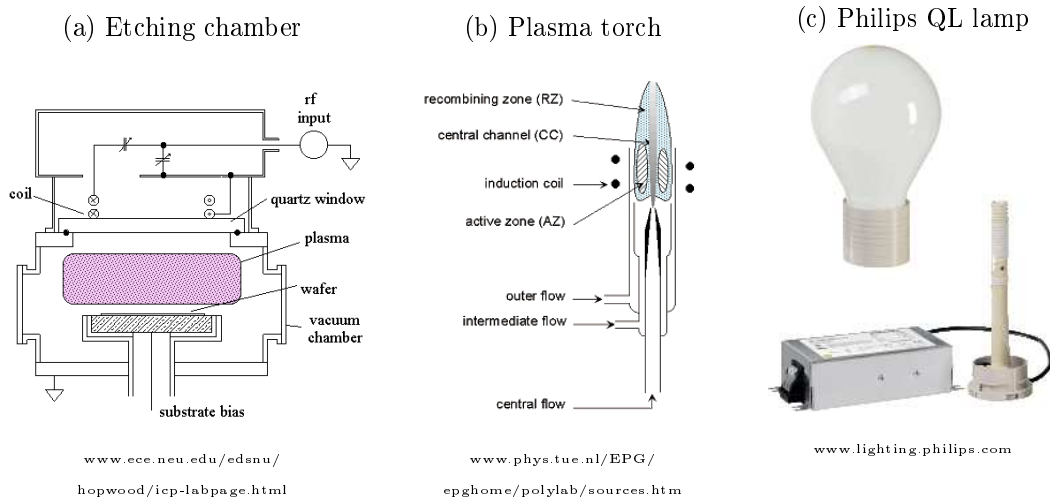


Figure 1.2: ICP devices in various applications. (a) Etching chamber: The plasma ions strike the substrate, etching grooves in the material. (b) Plasma torch: The sample gas is pumped through the inner channel, the plasma gas through the intermediate channel, and the insulating gas through the outer channel. (c) QL lamp: An inductive lamp consist of a closed bulb of gas that fits over a solenoid. The lifetime of these lamps is limited only by that of the electronics.

($\omega \gg \nu, kv_{Te}$), electrons do not move far during a single wave period and experience a local electric field. If the collision frequency is high ($\nu \gg \omega, kv_{Te}$), friction prevents the electrons from moving in a directed manner, so they again experience a local electric field.

If the thermal frequency is high ($kv_{Te} \gg \omega, \nu$), then the electrons sample the spatial variance of the electric field by moving through the skin layer. This causes the electric current to be non-locally dependent on the fields, and may result in an electron distribution that is non-Maxwellian and skin fields that do not decay exponentially. Linear theories can accommodate this complication, but only if the magnetic field is weak. Should a non-local plasma experience a low frequency wave, the magnetic field will produce non-linear trajectories which must be tracked via computer simulation.

1.2 Fundamentals

By assuming a local plasma with stationary ions, an ICP can be described by the electron fluid equation of motion and the Maxwell equations.

$$\begin{aligned}
m_e \frac{d\mathbf{v}}{dt} &= -e(\mathbf{E} + \mathbf{v} \times \mathbf{B}) - \nabla p - m_e \nu \mathbf{v} \\
\nabla \times \mathbf{E} &= -\frac{\partial \mathbf{B}}{\partial t} \\
\nabla \times \mathbf{B} &= \mu_0 \mathbf{J} + \frac{1}{c^2} \frac{\partial \mathbf{E}}{\partial t}
\end{aligned}$$

where m_e , \mathbf{v} , and ν are the electron mass, fluid velocity, and total collision rate, respectively. A number of simplifications can make this problem more tractable, starting with the assumption that all fields vary as $e^{i(kx - \omega t)}$. The pressure term can be dropped on the condition that the plasma density is close to uniform. Since the antenna is being driven at a low frequency ω , the displacement current is also insignificant and the electrons are able to keep up with the changes in the externally applied fields. To illustrate the basic properties, one can replace the equations with a linearized one-dimensional model along the \hat{z} axis.

$$\begin{aligned}
i\omega m \mathbf{v} &= -e\mathbf{E} - m\nu \mathbf{v} \\
\nabla \times \mathbf{E} &= i\omega \mathbf{B} \\
\nabla \times \mathbf{B} &= \mu_0 \mathbf{J}.
\end{aligned}$$

To find the dispersion equation, we start by combining the Maxwell equations.

$$\begin{aligned}
i\omega \mu_0 \mathbf{J} &= \nabla \times (\nabla \times \mathbf{E}) \\
&= \nabla(\nabla \cdot \mathbf{E}) - \nabla^2 \mathbf{E} \\
&= \mathbf{k}(\mathbf{k} \cdot \mathbf{E}) - k^2 \mathbf{E}
\end{aligned}$$

Since the EM wave is transverse, $\mathbf{k} \cdot \mathbf{E} = 0$, so the electric current is given by

$$\mathbf{J} = -n_0 e \mathbf{v} = \frac{ik^2}{\omega \mu_0} \mathbf{E}. \tag{1.1}$$

The electron fluid equation provides an alternative relation between the electron velocity and electric field.

$$\mathbf{v} = \frac{-ie\mathbf{E}}{m(\omega + i\nu)}. \tag{1.2}$$

Comparing these two equations, one arrives at the dispersion relation

$$c^2 k^2 = \frac{-\omega_{pe}^2 \omega}{\omega + i\nu}, \tag{1.3}$$

where $\omega_{pe} = (ne^2/\epsilon_0 m)^{1/2}$ is the plasma frequency. Letting $\nu \ll \omega$ gives the classical skin depth for a collisionless plasma.

$$\delta_c = \frac{1}{\Im(k)} = \frac{c}{\omega_{pe}} \quad (1.4)$$

To find the collisional skin depth, it is convenient to define [2]

$$\epsilon \equiv \tan^{-1} \frac{\nu}{\omega} \quad a \equiv \frac{\nu}{\omega} \quad \delta_0 \equiv \frac{c}{\omega_{pe}} (1 + a^2)^{1/4}. \quad (1.5)$$

This makes the dispersion relation

$$k^2 = \frac{-\omega_{pe}^2/c^2}{1 + ia} = \frac{-1}{\delta_0^2} \exp(-i\epsilon). \quad (1.6)$$

Then the classic collisional skin depth is found to be

$$\delta_s = \frac{1}{\Im(k)} = \delta_0 \sec(\epsilon/2) = \delta_c \sqrt{\frac{2(1 + a^2)}{1 + (1 + a^2)^{1/2}}}. \quad (1.7)$$

1.2.1 Anomalous Skin Effect

When eliminating the magnetic field from the Maxwell equations, it is implicitly assumed that the current is dependent only on the local electric field. However, if the mean free path of a thermal electron is long compared to the skin depth, $\lambda \gg \delta$, then most electrons will sample a varying electric field between infrequent collisions, making the current non-local. Therefore, when an ICP is run at low pressure, the observed skin depth is actually much longer than the classic collisional value.

In order to explain the anomaly in the observed skin depth, Pippard [7] pointed out that electrons that spend little time in the skin layer should not contribute significantly to the skin current because they have insufficient time to be accelerated by the skin field. Therefore, only those that enter at angles less than δ/λ (the ratio of skin depth to mean free path) make “effective” contributions to the current before colliding and returning to the plasma bulk. By assuming that the plasma conductivity is determined only by the effective electrons, the effective conductivity is

$$\sigma_{eff} = (\delta/\lambda)\kappa\sigma. \quad (1.8)$$

The equation for the electric current is transformed from $\mathbf{J} = \sigma\mathbf{E}$ to

$$\mathbf{J} = (\delta/\lambda)\kappa\sigma\mathbf{E} \quad (1.9)$$

Comparing this to Eq. (1.1), we can determine the skin depth resulting from this new

conductivity.

$$\frac{\delta}{\lambda} \kappa \sigma = \frac{ik^2}{\omega \mu_0} \quad (1.10)$$

By assuming that $\delta = 1/|k|$, the anomalous skin depth can be approximated as

$$\delta_a = \left(\frac{\lambda}{\omega \mu_0 \kappa \sigma} \right)^{1/3} \quad (1.11)$$

where κ is a numerical constant whose value is dependent on the electron distribution function. Weibel [15] finds it to be $\kappa = \sqrt{\pi}$ for a Maxwellian distribution.

1.2.2 Surface Impedance

The surface impedance is the ratio of the electric and magnetic fields on the surface of the plasma [8], $\zeta = \sqrt{\mu/\epsilon} = E_y/H_x$. The real component is related to the power flux, while the imaginary component gives the phase shift. In this problem, the power flux can be used to measure the energy absorbed by the plasma, which is important for maximizing the heating efficiency of the rf antenna. The reflection coefficient is given by

$$R_{\parallel} = \left| \frac{\zeta_0 - \zeta}{\zeta_0 + \zeta} \right|^2, \quad (1.12)$$

where $\zeta_0 = \sqrt{\mu_0/\epsilon_0}$ is the impedance of free space. In the limit that most energy is reflected, the absorbed power can be approximated by

$$P_{absorbed} = (1 - R_{\parallel}) P_{input} \approx 4 \frac{\zeta}{\zeta_0} P_{input}. \quad (1.13)$$

This treatment ignores the negligible amount of energy that passes completely through the finite length plasma and exits the far side.

Based on the theory of the anomalous skin effect in metals, Weibel solved the problem of a semi-infinite thermal plasma with electrons that are specularly reflected at the plasma boundary by substituting the Fermi electron distribution with a Maxwellian. His linear analysis [7] gives the surface impedance as

$$\zeta = -\frac{i\omega\lambda_{eff}}{\pi c} \int_{-\infty}^{\infty} \frac{dk}{k^2 + \Lambda Z(is/k)/k} (mks) \quad (1.14)$$

where $\lambda_{eff} = v_T/\sqrt{\nu^2 + \omega^2}$ is the effective mean free path, $s = \lambda_{eff}(\nu + i\omega)/v_T$, Z is the plasma dispersion function

$$Z(p) = \frac{1}{\sqrt{\pi}} \int_{-\infty}^{\infty} \frac{\exp(-x^2)}{x - p} dx, \quad (1.15)$$

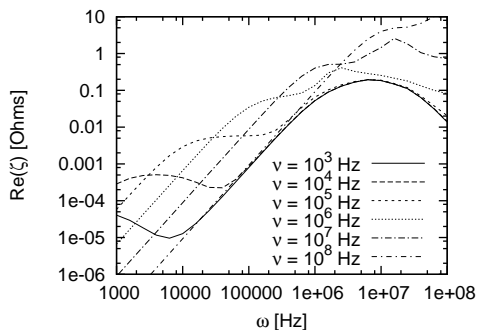


Figure 1.3: Example of using Eq. 1.17 to calculate the surface impedance for various driving and collision frequencies. The case of no collisions coincides with the minimum of all lines on the plot. When collisions are present, the impedance $\Re(\zeta)$, and hence power absorption, increases around the region where $\omega \approx \nu$. The system length is $L = 10$ cm and the probe depth is $x = 2$ mm.

and Λ is the non-locality parameter, given as

$$\Lambda = \left(\frac{\omega_p v_T}{c} \right)^2 \frac{\omega}{(\nu^2 + \omega^2)^{3/2}} = \frac{\lambda_{eff}^2}{\delta^2}. \quad (1.16)$$

Of course, no physical device is semi-infinite. A finite length plasma was first simulated by Turner [13]. Theory later developed by Shaing [10] gives the surface impedance as an infinite series of bounce modes

$$\zeta = \frac{4\pi i \omega}{c^2} \frac{2}{L} \sum_{n=0}^{\infty} \frac{1}{\phi_n^2 - \frac{\omega^2}{c^2} + i\alpha L k_n(a)}, \quad (1.17)$$

where $\phi_n = (2n + 1)\pi/2L$, $\alpha = 8\sqrt{\pi}n_e e^2 \omega / (M v_T c^2)$, and $k_n(a)$ describes the rate at which electrons cross the device relative to the driving frequency. When the collision frequency is independent of the electron energy, it is

$$k_n(a) = \int_0^{\infty} dy \exp(-y^2) \left[aL + \frac{(-1)^n (n + \frac{1}{2}) \pi y}{\sinh(aL/y)} \right] / \left\{ (aL)^2 + \left[\left(n + \frac{1}{2} \right) \pi y \right]^2 \right\}. \quad (1.18)$$

The first term in square brackets describes the wave-particle resonance in a semi-infinite system, while the second describes the resonance between the driving frequency and the wall bounce frequency. In the local limit, the wall bounce terms become insignificant and the equations recover Weibel's result.

1.2.3 Ponderomotive Force

Cold Plasma Approximation

When an EM wave impinges on a plasma, the electrons interact with the fields in such a way that they experience a force, called the ponderomotive or Miller force. In the simplest case, the ponderomotive force (PMF) can be found by considering the motion of a single particle. Unfortunately, without an electron energy distribution function, this precludes the possibility of describing a thermal plasma, but it is useful as a first step. The force is found by solving the electron equation of motion in oscillating electric and magnetic fields.

$$\begin{aligned} m \frac{d\mathbf{v}}{dt} &= -e(\mathbf{E} + \mathbf{v} \times \mathbf{B}) - m\nu\mathbf{v} \\ \mathbf{E}^{(1)} &= \mathbf{E}_s \cos \omega t \\ \mathbf{B}^{(1)} &= -\frac{1}{\omega} \nabla \times \mathbf{E}_s \sin \omega t \end{aligned}$$

In first-order, the Lorentz force disappears, so the velocity of the electron and its displacement are

$$\begin{aligned} \mathbf{v}^{(1)} &= -\frac{e}{m\omega} \mathbf{E}_s (1 + a^2)^{-1} (\sin \omega t + a \cos \omega t) \\ \mathbf{dr}^{(1)} &= \frac{e}{m\omega^2} \mathbf{E}_s (1 + a^2)^{-1} (\cos \omega t - a \sin \omega t), \end{aligned}$$

where $a = \nu/\omega$ is the collisionality parameter. Expanding $\mathbf{E}(\mathbf{r})$ around \mathbf{r}_0 , the second-order equation of motion is

$$m \frac{d\mathbf{v}^{(2)}}{dt} = -e \left[(\mathbf{dr}^{(1)} \cdot \nabla) \mathbf{E}^{(1)} + \mathbf{v}^{(1)} \times \mathbf{B}^{(1)} \right] - m\nu\mathbf{v}^{(2)} \quad (1.19)$$

which, after plugging in first-order values, produces

$$\begin{aligned} \frac{d\mathbf{v}^{(2)}}{dt} + \nu\mathbf{v}^{(2)} &= -\frac{e^2}{m^2\omega^2} \frac{1}{1 + a^2} \left[(\cos^2 \omega t - a \sin \omega t \cos \omega t) \mathbf{E}_s \cdot \nabla \mathbf{E}_s \right. \\ &\quad \left. + (\sin^2 \omega t + a \sin \omega t \cos \omega t) \mathbf{E}_s \times (\nabla \times \mathbf{E}_s) \right] \end{aligned}$$

The final term can be modified by

$$\mathbf{E}_s \times (\nabla \times \mathbf{E}_s) = \frac{1}{2} \nabla \mathbf{E}_s^2 - (\mathbf{E}_s \cdot \nabla) \mathbf{E}_s, \quad (1.20)$$

but in a transverse wave, the intensity varies in the direction of the wave vector, which is perpendicular to the electric field polarization. Therefore, the terms involving the gradient

of the electric field disappear and the ponderomotive force takes the form

$$\mathbf{F}_{NL} = -\frac{\omega_{pe}^2}{\omega^2} \frac{1}{1+a^2} \frac{\epsilon_0}{2} \nabla \langle E^2 \rangle (1 - \cos 2\omega t + a \sin 2\omega t) \quad (1.21)$$

in a plasma with no thermal motion.

Thermal Plasma Linear Approximation

The added complexity of a thermal distribution of electron velocities requires that the equations be linearized and the magnetic field be ignored. The solution of the PMF under these conditions has been accomplished in two different ways.

Smolyakov *et al.*[11] assumes that the electric and magnetic fields are prescribed by decaying exponentials in the skin layer. While the fields in the skin are known to be non-monotonic, they usually become so deep inside. Therefore, the approximation should be accurate where the PMF is largely. The field profiles are defined as

$$\begin{aligned} E_y(z, t) &= E_0 \exp(-\gamma z) \exp(-i\omega t) \\ B_x(z, t) &= \frac{i\gamma}{\omega} E_0 \exp(-\gamma z) \exp(-i\omega t), \end{aligned}$$

where E_0 is the field amplitude at the plasma boundary, $\gamma = 1/\delta - i\xi$ is the complex longitudinal wave number, δ is the skin depth, and ξ determines the energy flux into the plasma. The calculated PMF is found to be

$$F_p = \frac{\omega_p^2}{8\pi\omega} E_0^2 \exp\left(-\frac{2z}{\delta}\right) \Re \left\{ i \frac{\gamma^*}{\gamma v_T} [Z(-is) - \exp(\gamma z) G(\gamma z, s)] \right\}, \quad (1.22)$$

where Z is the plasma dispersion function (Eq. 1.15), $s = (\omega + i\nu)/\gamma v_T$, and

$$G(\gamma z, s) = \frac{2}{\sqrt{\pi}} \int_0^\infty \frac{t \exp(i\gamma z s/t - t^2)}{t^2 + s^2} dt. \quad (1.23)$$

The alternative approach is to use Shaing's model in which the fields are calculated self-consistently. The magnetic field and electron current are found to have complex amplitudes given by

$$\begin{aligned} B_x(z) &= -i \frac{2\mu c}{\omega L} \sum_{n=0}^{\infty} \frac{\phi_n \sin(\phi_n z)}{\phi_n - \frac{\omega^2}{c^2} + i\alpha L k_n(a)} \\ J_y(z) &= \frac{-i\mu c^2}{2\pi\omega L} \sum_{n=0}^{\infty} \frac{\left(\phi_n^2 - \frac{\omega^2}{c^2}\right) \cos(\phi_n z)}{\phi_n^2 - \frac{\omega^2}{c^2} + i\alpha L k_n(a)}, \end{aligned}$$

where ϕ_n , α , and $k_n(a)$ are defined as before and $\mu = -dE_y/dz|_{z \rightarrow 0^+}$ is the rate of change of

the electric field near the plasma boundary. While he just solves for the surface impedance, they can also be used to find the ponderomotive force from the equation

$$F_p = -\frac{1}{2c} |J| |B| \cos(\phi_J - \phi_B), \quad (1.24)$$

where the angles are found from the identity $A = |A| \exp(i\phi_A)$. This can be simplified to

$$F_p = -\frac{1}{2c} [\Re(J)\Re(B) + \Im(J)\Im(B)] \quad (1.25)$$

Unfortunately, when $x \ll L$, the summation for the magnetic field diverges because it is not continuous in the infinite periodic system, so the Gibbs phenomenon occurs. [1] However, a rigorous workaround has been developed by Yoon *et al.* [16], which I am in the process of implementing.

CHAPTER 2

SIMULATION

2.1 Motivation

ICP devices are used for many applications, and while the underlying physics is classical electromagnetism, the full effects resulting from Maxwell's equations are not fully understood. Even the most complex analytical models for low-pressure ICP [10, 11] use linear models for simplicity. Therefore, the ponderomotive force and surface impedance cannot be calculated in the regimes where they are significant, such as when the plasma is driven at low frequency. Using computer simulations will give us a more accurate picture of the phenomena that occur under all conditions. In addition, by running simulations that cover a large portion of parameter space and subsequently build in complexity, it is hoped that we can ascertain the source of each effect, be it the nonlinear fields, mobile ions, or collisions with neutral atoms.

Before the full nonlinear dynamics are investigated, the first goal of the project must be to determine that the simulation corroborates the results of the linear theories. The process of linearization disregards two real effects, the magnetic field and the longitudinal electric field. The magnetic field comes from the EM wave and causes the particle trajectories to be curved. The longitudinal electric field occurs because the electrons are accelerated more quickly in response to the ponderomotive force than the ions. This creates a charge separation normal to the plasma surface that is counteracted by the longitudinal field. These effects are difficult to analyze, so linear theories require that all particles travel in straight lines and are not accelerated normal to the surface, so that they spend a predictable length of time in the skin layer. To accomplish this in the simulation, the magnetic and longitudinal electric fields are simply zeroed out and ignored.

2.2 1d2v Electromagnetic Model

The description of ICP in plane slab geometry is covered in a number of sources[1]. The following advective algorithm was developed by Dawson and Langdon. Assuming that the impinging EM wave is traveling normal to the surface of the plasma, and denoting that

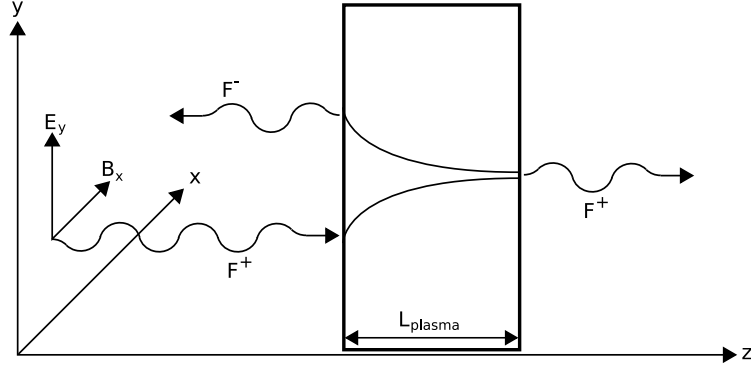


Figure 2.1: The electromagnetic fields are simulated in one-dimension as the superposition of an incoming wave F^+ and a reflected wave F^- .

direction as \hat{z} , we model a plasma with slab geometry, homogeneous in the \hat{x} and \hat{y} directions. Maxwell's equations can then be simplified to

$$\frac{\partial B_x}{\partial z} = \mu_0 J_y + \frac{1}{c^2} \frac{\partial E_y}{\partial t} \quad (2.1)$$

$$\frac{\partial E_y}{\partial z} = -\frac{\partial B_x}{\partial t} \quad (2.2)$$

Because there is no electric field in the \hat{x} direction, and no magnetic field in the \hat{y} and \hat{z} directions, only the \hat{y} and \hat{z} components of velocity need to be recorded for each particle. Therefore, the model is “1d2v,” signifying the number of position and velocity variables under consideration, in this case: z , v_y , and v_z .

Adding and subtracting the Maxwell equations permits the introduction of a quantity for waves travelling forwards (F^+) versus those travelling backwards (F^-).

$$F_y^\pm = \frac{1}{2}(E_y \pm cB_x) \quad (2.3)$$

The wave equation becomes

$$\left(\frac{\partial}{\partial t} \pm c \frac{\partial}{\partial z} \right) F_y^\pm = -\frac{1}{2} \frac{J_y}{\epsilon_0}. \quad (2.4)$$

Boundary conditions are based on the assumption that the plasma is surrounded by vacuum, with a wave impinging from the left. In the vacuum (Fig. 2.1), the magnitude of the magnetic field is related to that of the electric field by Faraday's law, so that $E_y = cB_x$. By plugging this into the identity for F^+ , we see that the left boundary condition is

$$F^+(z = 0, t) = E_{drive} \sin(\omega t) = cB_{drive} \sin(\omega t), \quad (2.5)$$

while at the right boundary, there is no incoming wave.

$$F^-(z = L_{pl}, t) = 0 \tag{2.6}$$

The advantage of recording F^\pm instead of the actual electric and magnetic fields is that propagation simply requires shifting the values of F^+ to the right and those of F^- to the left. By setting the time step $\Delta t = c\Delta x$, the shift becomes exactly one mesh element. While this is computationally simple, such a small time step requires long runs. However, numerical instability is of little concern, since the Courant factor is equally small.

2.3 Particle-in-Cell Algorithm

The obvious method of modelling the dynamics of an N-body system is via a particle-particle algorithm, where each particle interacts with all others, as it does in reality. However, this requires computation time on the order of $\mathcal{O}(N^2)$ and hence, limits the number of particles that can be handled feasibly by the simulation. It is much more efficient to project all the particle properties $\mathcal{O}(N)$ onto an M-celled grid on the \hat{z} axis, find the resulting force fields on the mesh $\mathcal{O}(M)$, and interpolate those forces back to the particles $\mathcal{O}(N)$. Such a system is called a particle-mesh (PM) or particle-in-cell (PIC) algorithm and is particularly useful when electromagnetic fields are involved, since the grid is already required to store the spatial dependence of those fields.

2.3.1 Sequence of a Time Step

For this description of system evolution, it is useful to follow along in Fig. 2.2. To find the state of the particle system at the $(n + 1)^{th}$ time step, we start with the particle positions z^n and the transverse electric and magnetic fields E_y^n, B_x^n at the current time step n , as well as the particle velocities $v^{n-1/2}$ at the $(n - \frac{1}{2})^{th}$ half-step. The positions and velocities are half a time step out of sync so that each can be advanced using the time-averaged value of the other. This increases the stability and accuracy of the evolution.

Step (1) involves projecting the particle moments onto the mesh. The properties of each particle are weighted among the nearby cells to find the charge density, temperature, and current on the mesh. For my program, the weighting is linear between the two adjacent cells. The statistical noise in a PIC simulation is approximately $\sqrt{M/N}$, inversely related to the number of particles occupying each cell. With a large number of particles per cell, each one will represent less charge and cause a smaller fluctuation when passing between cells. I usually run with 10000 particles per cell, limiting stochastic error to less than 1%.

Step (2) is using the mesh values to find the longitudinal electric field. In a charged plasma or one driven at high-frequency, Poisson's equation is used to calculate the field

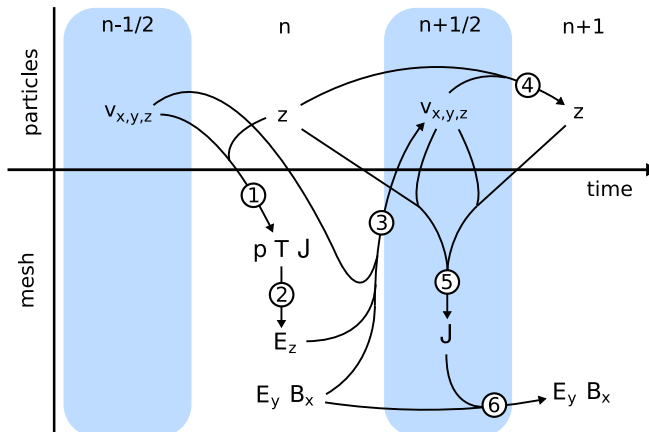


Figure 2.2: A pictorial representation of the steps required to advance the simulated plasma one increment in time. All quantities shown above the horizontal line are particle properties. These include only the velocity $v_{x,y,z}$ and position z . The quantities below the line are mesh properties, which include the plasma density ρ , temperature T , and current J , longitudinal electric field E_z , and transverse fields E_y and B_x . A description of each numbered step can be found in Section 2.3.1. A linear simulation does not include Step (2).

from the charge density. However, when the plasma is quasineutral, it is highly susceptible to the stochastic noise from the PIC simulation. Therefore, a quasineutral approximation, described in Sec. 2.5, is used. It reduces noise and is computationally faster than Poisson's equation, which requires solving coupled equations.

Step (3) interpolates the fields on the mesh, E_y , E_z , and B_x , to the particles by linearly weighting the values at the two nearest cells. Then each particle is accelerated via the Lorentz force. The most efficient methods for performing the acceleration calculation are described in Birdsall and Langdon 4-3, but all are mathematically equivalent to the centred-difference form

$$\frac{\mathbf{v}^{n+1/2} - \mathbf{v}^{n-1/2}}{\Delta t} = \frac{q}{m} \left[\mathbf{E} + \frac{\mathbf{v}^{n+1/2} + \mathbf{v}^{n-1/2}}{2} \times \mathbf{B} \right]. \quad (2.7)$$

If there are electron-neutral collisions, they are performed at the end of this step to randomize the recently calculated velocities.

Step (4) moves each particle based on its new velocity. If a particle hits an edge of the plasma, it is specularly reflected. Using both the old and new positions, as well as the new velocities, Step (5) evaluates the electric current centred both in space, between cells, and in time, at step $(n + \frac{1}{2})$.

The task of the last step, Step (6), is to update the transverse electric fields to the time $(n + 1)$. However, besides simple propagation of the left-going wave moving left and the

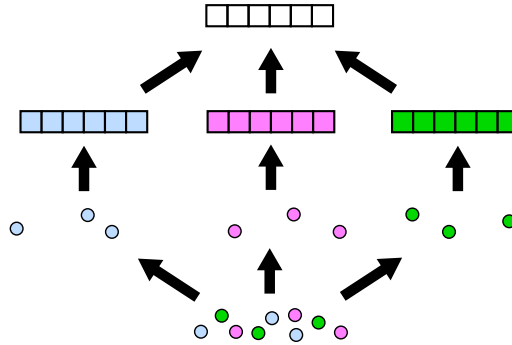


Figure 2.3: Representation of the work allocation among multiple processors. The plasma particles and their resultant fields are divided among all CPUs (represented by different colours), but the fields are superposed at each time step before the particle motion is updated.

right-going wave going right, the plasma currents modify the amplitude. The currents are recorded at positions directly between the mesh cells, so that when the EM fields cross them to reach the next cell, the left- and right-going waves are influenced by the same amount. Once this step is complete, the cycle begins again.

2.4 Parallelization

To divide the work of the simulation among multiple CPUs, after the particles are initialized, they are randomly distributed to each task. Then each task independently tracks the motion of its own group, and calculates the mesh properties (density, temperature, current, etc.) of only those particles. Since the fields on the mesh can be superposed, they are summed over all tasks and the answer is broadcast back to each CPU. This occurs between Steps (2) and (3) in Fig. 2.2 and is visually represented in Fig. 2.3.

Once each CPU has the complete set of particle moments, they all perform the same calculation of the new fields. This is certainly inefficient behaviour, but the mesh is much smaller than the number of particles, even the number of particles on single CPU, so it comprises a small addition to the total work. The proper method would be to partition the mesh out among the processors as well. This would be quite difficult, however, because some properties, notably the temperature, are spatially smoothed, required additional communication among tasks about the values at the division edge. The gained efficiency would not offset the complexity of the necessary changes to the program.

After the electric fields have been found using the collected mesh values, each task interpolates the values back to its group of particles and adjusts their motion accordingly. This process is repeated at each step.

2.5 Quasineutral Approximation

The PMF accelerates the electrons much more rapidly than the ions, causing a charge separation in the longitudinal direction. To maintain plasma neutrality, a longitudinal electric field arises to compensate. Ordinarily, the field is calculated using Poisson's equation, but if a plasma is quasineutral, as is the case when it is driven by a low-frequency wave, the density fluctuations are small and mostly stochastic, due to the limited number of particles in a numerical simulation. Such behaviour produces a noisy longitudinal electric field. An alternative technique has been developed empirically by Joyce *et al*[5]. We start with the electron fluid equation of momentum conservation

$$m_e n_e \frac{d\mathbf{u}}{dt} = -en_e (\mathbf{E} + \mathbf{u} \times \mathbf{B}) - \nabla \cdot \mathbf{P}, \quad (2.8)$$

where m_e , n_e , and \mathbf{u} are the electron mass, density, and fluid velocity, and \mathbf{P} is the pressure tensor given by

$$\mathbf{P} = \int d^3v m_e \mathbf{v} \mathbf{v} f(\mathbf{x}, \mathbf{v}, t) \equiv n_e T_e(\mathbf{x}, t) \quad (2.9)$$

For the one-dimensional problem, we only need the \hat{z} component, which is

$$m_e n_e \frac{du_z}{dt} = -en_e (E_z - u_y B_x) - \frac{\partial}{\partial z} (n_e T_{ez}) \quad (2.10)$$

Solving this for the electric field gives

$$E_z = -\frac{J_y B_x}{en_e} - \frac{1}{en_e} \frac{\partial}{\partial z} (n_e T_{ez}) - \frac{m_e}{n_e} \frac{du_z}{dt}, \quad (2.11)$$

where the current is $J_y = -en_e u_y$. The first two terms represent the ambipolar electric field, while the last inertial term is responsible for maintaining quasineutrality. The problem is that the last term is negligible compared to the others, so the electron acceleration is essentially random. To fix this, the electric field is modified to artificially increase the charge separation perceived by the electrons.

$$\begin{aligned} E_z &= -\frac{J_y B_x}{en_e} - \frac{1}{en_e} \frac{\partial}{\partial z} (n_e T_{ez}) + \left[\frac{1}{en_i} \frac{\partial}{\partial z} (n_i T_{ez}) - \frac{1}{en_i} \frac{\partial}{\partial z} (n_i T_{ez}) \right] - \frac{m_e}{n_e} \frac{du_z}{dt} \\ &= -\frac{J_y B_x}{en_e} - \frac{1}{en_i} \frac{\partial}{\partial z} (n_i T_{ez}) + \left[\frac{1}{en_i} \frac{\partial}{\partial z} (n_i T_{ez}) - \frac{1}{en_e} \frac{\partial}{\partial z} (n_e T_{ez}) - \frac{m_e}{n_e} \frac{du_z}{dt} \right] \end{aligned}$$

Letting the sum in the brackets be equal to zero, the new electric field will cause the electrons to accelerate towards regions where the ion density is higher than the electron density.

$$m_e \frac{du_z}{dt} = T_{ez} \frac{\partial}{\partial z} \ln \left(\frac{n_i}{n_e} \right) \quad (2.12)$$

Because the acceleration has been greatly increased, the electrons will oscillate around regions of positive charge density. This under-relaxation means that there is no need to time-centre the calculation, but the electric field must be smoothed to damp out these high-frequency oscillations. This scheme is purported to have excellent stability and energy conservation properties.

2.6 Collisions

The only type of interaction to be used in these simulations is the Monte Carlo electron-neutral elastic collision. Because the neutral atoms are not tracked in this simulation, the method for imitating electron-neutral collisions[14] involves randomly choosing electrons and selecting their angular change in velocity from a distribution. A colliding electron has an equal probability of being scattered in any perpendicular direction. Therefore, the azimuthal direction ϕ (Fig. 2.4) is uniformly distributed on the interval $[0, 2\pi]$, with the value given by

$$\phi = 2\pi R_1, \quad (2.13)$$

where R_1 is a random number in the range $[0, 1]$.

The scattering angle is dependent on the energy of the incident electron ε . A large energy should result in a small forward scattering angle, while a small energy should produce an isotropic distribution. The approximate differential cross section that gives this behavior is

$$\frac{\sigma(\varepsilon, \chi)}{\sigma(\varepsilon)} = \frac{\varepsilon}{4\pi [1 + \varepsilon \sin^2(\chi/2)] \ln(1 + \varepsilon)}. \quad (2.14)$$

To randomly generate the angle χ from this equation, one must solve

$$R_2 = \frac{\int_0^\chi \sigma(\varepsilon, \chi) \sin \chi d\chi}{\int_0^\pi \sigma(\varepsilon, \chi) \sin \chi d\chi} \quad (2.15)$$

to arrive at

$$\cos \chi = \frac{2 + \varepsilon - 2(1 + \varepsilon)^{R_2}}{\varepsilon}. \quad (2.16)$$

The direction ϕ and scattering angle χ are then used to find the scattering vector in the lab

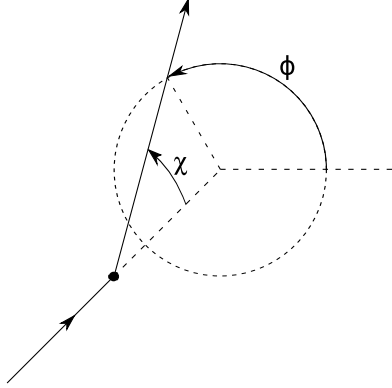


Figure 2.4: In the centre of mass frame, an electron comes in from the lower-left and collides with a stationary neutral (black dot). The electron is deflected by angle χ from its original path. The direction of deflection ϕ is isotropic.

frame according to

$$\hat{v}_{scat} = \hat{v}_{inc} \cos \chi + \hat{v}_{inc} \times \hat{\mathbf{i}} \frac{\sin \chi \sin \phi}{\sin \theta} + \hat{v}_{inc} \times (\hat{\mathbf{i}} \times \hat{v}_{inc}) \frac{\sin \chi \cos \phi}{\sin \theta}, \quad (2.17)$$

where θ is the angle of incidence relative the coordinate system, given by $\cos \theta = \mathbf{v}_{inc} \cdot \hat{\mathbf{i}}$.

Since there is such a dichotomy between the mass of the electron m and neutral atom M , there is not much energy transferred in the collision. The change, rarely more than 1%, is given by

$$\Delta \varepsilon = \frac{2m}{M} (1 - \cos \chi). \quad (2.18)$$

The power created through collisions is much less than that delivered to the plasma by the rf antenna, so it is ignored when calculating energy absorption.

According to linear theories, it is expected that the inclusion of electron-neutral collisions will enlarge the regime where the surface impedance is non-negligible (Fig. 1.3). This remains to be implemented and tested in the PIC simulation.

CHAPTER 3

RESULTS

3.1 Program Scalability

The original PIC program used to generate the described data was written by D. Sydorenko[12] at the University of Saskatchewan for his Ph.D thesis. I parallelized it using MPI to run on multiple processors simultaneously. The reason we wish to run on multiple processors is obviously to gain a speed-up in computation time. The speed-up is a simple quantity to determine, as we just need to run the program with different numbers of CPUs and tabulate the results as $T(1)/T(p)$, where $T(p)$ is the time taken for p processors to complete the simulation. One can see in Table 3.1 that the speed-up is generally greater when there are more particles involved. This is because particle manipulation does not involve interprocessor communication.

Unfortunately, the speed does not increase linearly as processors are added. One would expect that more processors would decrease proportionately the time required to execute a program, but there is also more communication overhead, usually proportional to $\log p$, where p is the number of processors. Therefore, a more frequently used measure of parallel performance is the efficiency, the total CPU time required for p parallel processors to complete a run relative to that of a serial calculation.

$$E = \frac{T(1)}{pT(p)} \tag{3.1}$$

The disadvantages of looking at only the efficiency is that the reason for decreasing efficiency is not quickly apparent. Therefore, Karp and Flatt[6] describe another metric that can identify the cause of lost efficiency, the serial fraction. If the time to run the program is

$$T(p) = T_s + \frac{T_p}{p}, \tag{3.2}$$

where T_s is the time taken for serial calculation and T_p the time that it runs perfectly parallel. By noting that $T(1) = T_s + T_p$ and defining the serial fraction as $f = T_s/T(1)$, it

	2.5×10^5 particles	10^6 particles	4×10^6 particles
serial run time	2608 s	10367 s	41474 s
2 processors	1.96	1.94	1.98
3 processors	2.58	2.95	2.94
4 processors	3.23	3.95	3.90
5 processors	3.88	4.88	4.84
8 processors	5.42	7.58	7.68
9 processors	5.78	8.57	8.65
16 processors	13.80	14.44	15.20
17 processors	13.94	15.40	16.17
32 processors	22.29	28.32	29.41
33 processors	22.29	29.12	28.56

Table 3.1: The serial run time and speed-up rates for a for a program running with nonlinear dynamics on a 100 cell mesh. A speed-up of 2 indicates the program completed twice as fast as a serial run.

can be written

$$f = \frac{T(p)/T(1) - 1/p}{1 - 1/p}. \quad (3.3)$$

This parameter can give details about the scalability that the efficiency does not show. For instance, an abrupt change in f results from load-balancing effects, while a smooth increase results from communication overhead.

From the data found in Fig. 3.1, one can see that the efficiency improves with the number of particles, but drops secularly as the number of processors is increased. This runs counter to the theory that communication varies as $\log p$, and suggests that there may be bottlenecks in the network. Despite the high efficiency for few processors, the serial fraction shows that there is much more time spent waiting due to load imbalances than when many processors are used. As the number of particles is increased, the load imbalances become less significant and the serial fraction plot is smoother. I believe the reason for the slow decrease in serial calculation is due to the repetition of mesh calculations over all processors. As the processor number is increased, the mesh calculations become less significant relative to the communication overhead. If a much greater number of processors were used, the serial fraction would increase as it should because the communication would be the dominant hindrance to fully parallel calculation.

In general, with many particles the serial fraction is low and the efficiency is high. Therefore, in the regime where $N \gg M$, the number of processors can be essentially arbitrary. Since most of the simulations are run with 200 cells and 2 million particles, I do not worry about the processor number based on efficiency, but on my allocation of resources. From experience, usually a low number is advantageous when in competition for resources with other users.

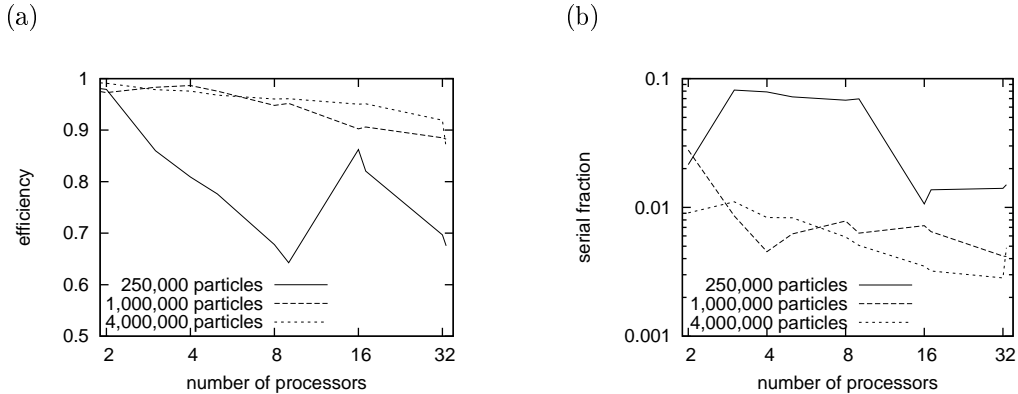


Figure 3.1: Parallel performance metrics for a nonlinear simulation performed on a 100 cell mesh. (a) As the number of particles is increased, the efficiency becomes better with the processors spending less time waiting for one another. (b) The serial fraction of runs with low particle counts varies less smoothly than those with high particle counts, because they are more susceptible to load-balancing inefficiencies.

3.2 Skin Depth

Since the fields in the skin-layer are non-monotonic [15, 7, 2], it is difficult to measure their exact depth. An example is shown in Fig. 3.2. For the parameters shown, the theoretical value of the classical collisionless skin depth is 1.7 cm, while the anomalous skin depth is 3.1 cm. While both are the correct order, one can see how difficult it is to determine the actual skin depth for comparison. Weibel uses the technique of defining the skin depth as it would be if the decay rate of the electric field did not change from its value at the plasma boundary.

$$\delta = \frac{dz}{d(\ln(E_y(z)))} \Big|_{z=0} \quad (3.4)$$

This formula gives the skin depth for this case at 2.5 cm. While this does appear accurate at small depths, it is questionable in the deeper region where the field is obviously not decaying exponentially.

3.3 Surface Impedance

Comparing the surface impedance from Shaing’s theory with the linear dynamics simulation, one can see that the agreement is excellent (Fig. 3.3), except for some unusual effects in the real part of the impedance at high frequency. The plasma is highly reflective at high and low frequencies, but becomes absorptive near the resonant Landau frequency, and the impedance is independent of the amplitude of the driving electric field.

Once one includes the nonlinear dynamics in the program, however, the transition from

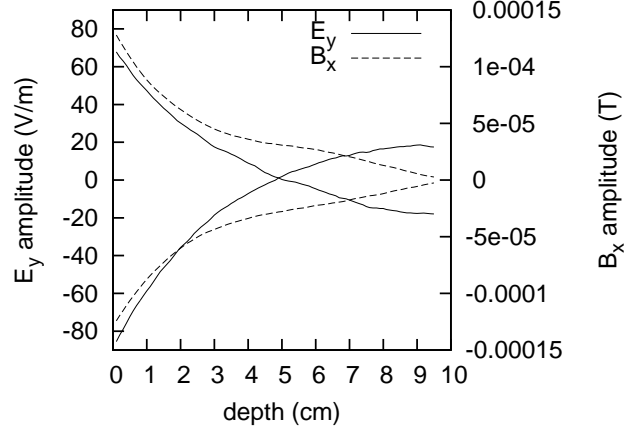


Figure 3.2: Skin field envelopes for a nonlinear simulation with immobile ions and plasma parameters $\omega_{drive} = 4$ MHz, $E_{drive} = 2 \times 10^5$ V/m, $n = 10^{17}$ cm $^{-3}$, $L_{pl} = 10$ cm, and $T_e = 10$ eV.

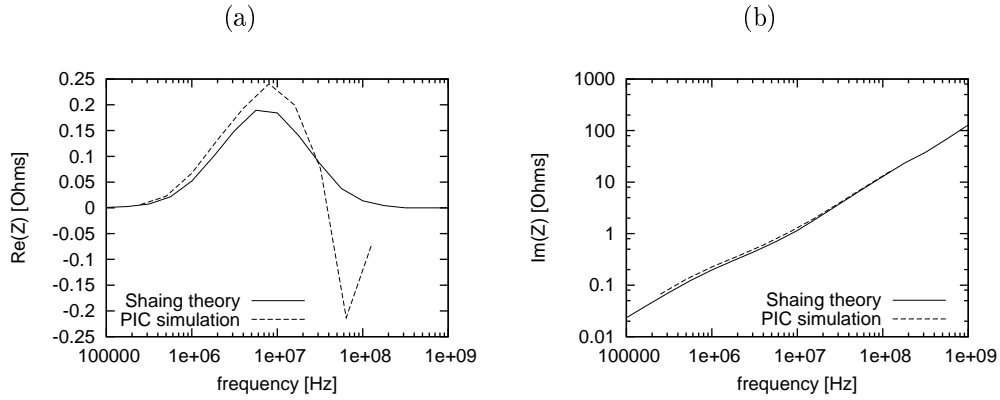
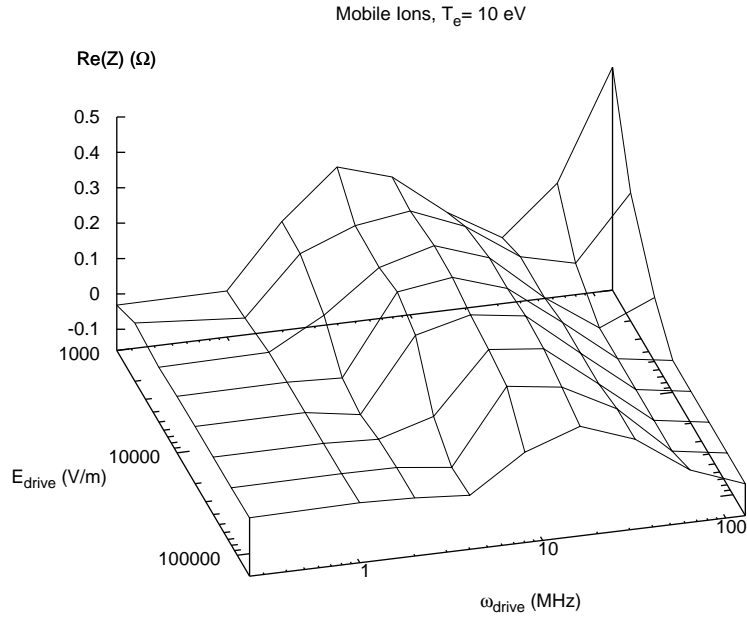


Figure 3.3: The (a) real and (b) imaginary components of the surface impedance from a simulation with linear dynamics compared with the Shaing formula for collisionless surface impedance. Plasma parameters are $n = 10^{17}$ cm $^{-3}$, $L_{pl} = 10$ cm, and $T_e = 10$ eV.

(a)



(b)

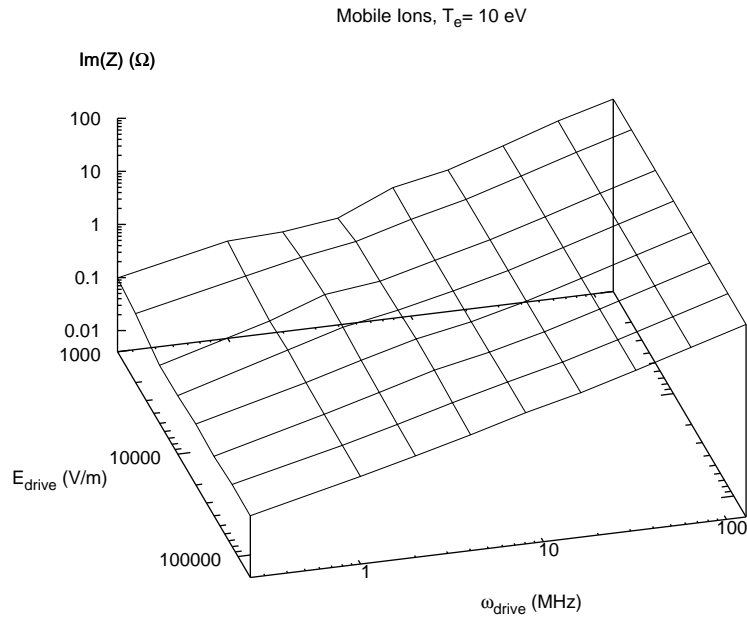


Figure 3.4: The (a) real and (b) imaginary components of the surface impedance versus frequency and amplitude. This simulation includes nonlinear dynamics and a mobile ion species with $m_i/m_e = 74400$. Plasma parameters are $n = 10^{17} \text{ cm}^{-3}$, $L_{pl} = 10 \text{ cm}$, $T_e = 10 \text{ eV}$ and $T_i = 1 \text{ eV}$.

a completely reflective plasma to an absorptive one becomes much sharper. Also visible in Fig. 3.4 is the fact that both the transition frequency and phase shift become dependent on the strength of the incoming wave. Some unexpected behaviour continues to appear in the high-frequency region, as in the linear simulation.

The immediate objective is to include electron-neutral collisions in the calculations. Currently the surface impedance becomes small away from the Landau resonant frequency, which would not occur in reality because the particle collisions would become the dominant mechanism of heat dissipation (Fig. 1.3).

3.4 Ponderomotive Force

When using linear dynamics, the PMF is found to be proportional to the square of the transverse electric field, as expected (Fig. 3.5a). However, thermal motion causes the PMF at low frequency to be less than would be expected in a cold plasma, as shown by linear simulations and theory (Fig. 3.5b). This is because hot particles pass through the skin layer more quickly than cold ones, and so are influenced by the fields for more briefly.

When the magnetic and longitudinal electric fields are included, the PMF retains its simple exponential relationship with the electric field, but the exponent is not the cold plasma value of 2. This was known from data acquired with the original serial PIC simulation (Fig. 3.5c). However, it was believed that at low driving amplitudes, the relationship would return to the cold plasma approximation, regardless of temperature. With the parallel program, the regime of very low driving amplitude (<1 V/m) became accessible. It can be seen that there is no change in the PMF between high and low amplitudes. This new effect works to counteract the suppression of the PMF caused by thermal motion (Fig. 3.5d).

It is interesting to see how the value of the exponent relating the electric field in the plasma skin to the ponderomotive force changes with temperature. Using the cold plasma relationship as a baseline, the slope increases with the logarithm of the temperature (Fig. 3.5e) as

$$F_{PM} \propto E_y^{2+\alpha \log(T/T_0)}. \quad (3.5)$$

This expression only holds when the temperature is above a critical temperature T_0 , where the exponent becomes greater than 2. Otherwise, the relationship is the same as that in a cold plasma. It is postulated that the temperature T_0 is significant because the transit time of a thermal electron through the skin becomes comparable to the rf driving period $v_T/\delta \omega$. At a driving frequency of $\omega = 0.5$ MHz, I have found the slope relating the temperature to the PMF to be $\alpha = 0.041$. Calculating the skin depth using this criterion, the critical temperature at which the fitted line intersects the x -axis is $T_0 = 3.4 \times 10^{-2}$ implies a skin depth of roughly 5 cm. In actuality, the skin depth for this case is 2 cm. More data is being

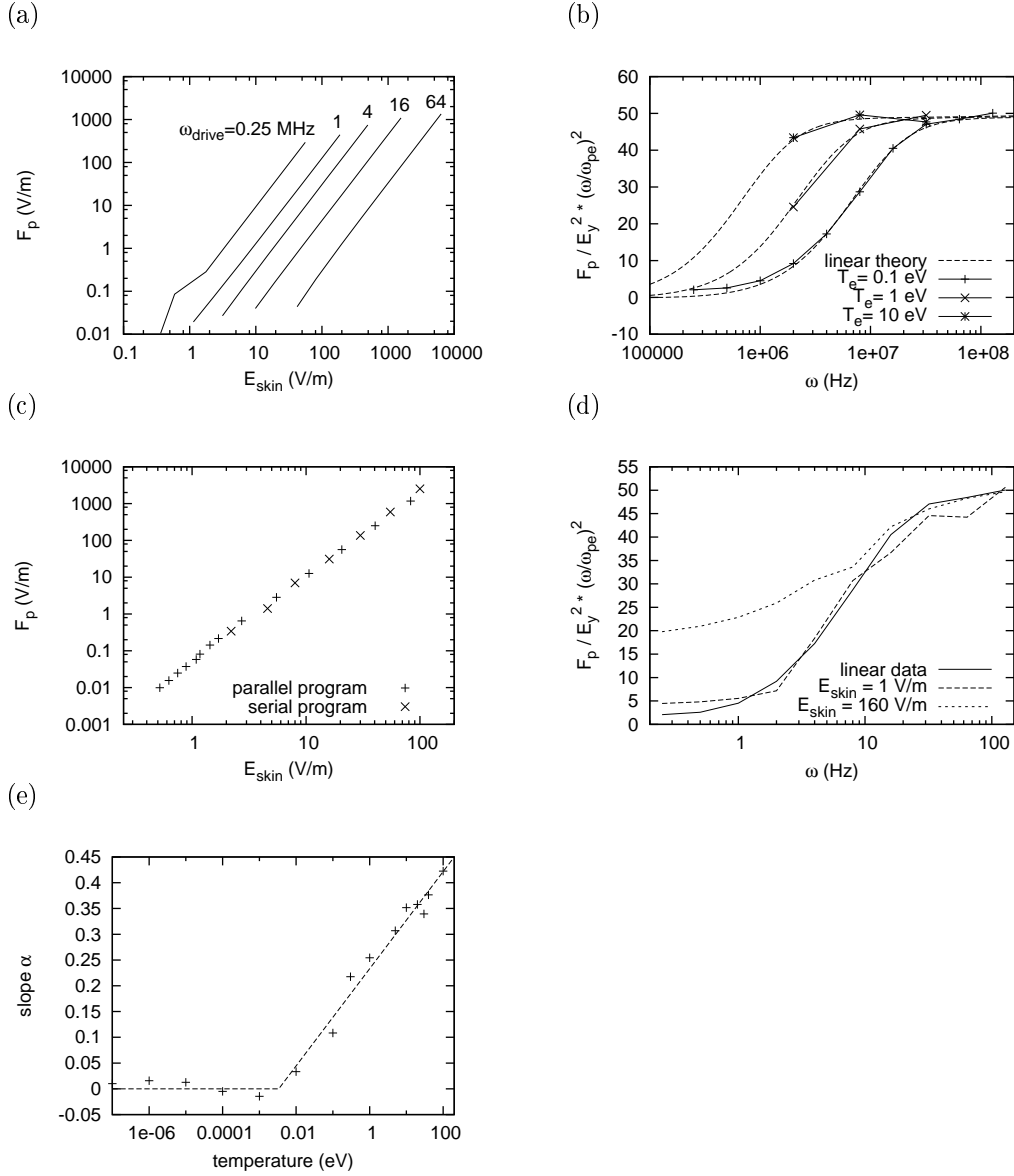


Figure 3.5: (a) When using linear dynamics, the PMF is proportional to the square of the electric field in the skin, independent of frequency. This plot shows the PMF for frequencies of 0.25, 1, 4, 16, and 64 MHz. (b) For a skin depth of 2 cm, the cold plasma approximation suggests the PMF coefficient should be 50. In a thermal plasma, the PMF is reduced at low frequency, confirmed by tests and Eq. (1.22). (c) When nonlinear dynamics are included, the PMF becomes proportional to a different power of the electric field at high temperature. The power is independent of the amplitude of the driving wave. This data for $\omega = 0.5$ MHz and $T_e = 10$ eV fits well to $F_p \propto E_{skin}^{2.3}$. (d) As the amplitude is increased, the nonlinear dynamics compensates for the thermal reduction in PMF at $T_e = 10$ eV. (e) The relationship between the PMF and electric field changes with the temperature. This is expressed by Eq. (3.5) with α proportional to the logarithm of the temperature above a critical point and zero otherwise.

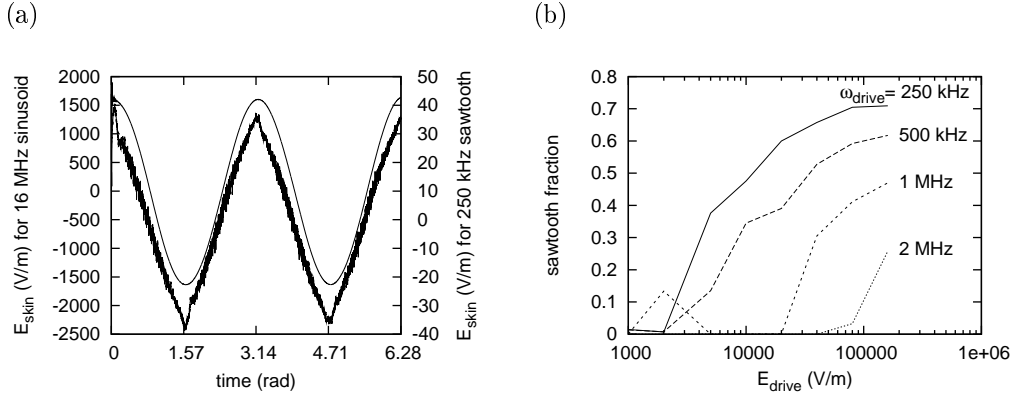


Figure 3.6: (a) At high frequencies, the transverse electric field in the skin is sinusoidal, but as the frequency decreases, it becomes a sawtooth. Examples of each are shown when the driving field has amplitude $E_{drive} = 160$ V/m. (b) Fitting to a superposition of pure sinusoid and sawtooth shows the fraction of the amplitude that is due to higher order harmonics. The simulations include nonlinear dynamics with plasma parameters $n = 10^{17}$ cm $^{-3}$, $L_{pl} = 10$ cm, and $T_e = 10$ eV.

produced to determine the cause of the discrepancy.

3.5 High-Order Harmonics

Godyak [4] describes observing the appearance of a spectra of higher order harmonics of the longitudinal electric field in a cylindrical ICP. These simulations show harmonics that appear in the transverse electric field of planar ICP. Fig. 3.6a shows an example of the difference in form between the field at low frequency versus at high. To find a regime for this phenomenon, rather than testing each harmonic separately to find a spectrum, I add together a pure sinusoid with a pure sawtooth using a variable mixing fraction. The fit takes the following form.

$$E_y(z = 2 \text{ mm}, t) = E_0 \left[(1 - b) \cos \omega t + b \left(\frac{2}{\pi} \sin^{-1}(\cos \omega t) \right) \right], \quad 0 < b < 1, \quad (3.6)$$

where E_0 is the maximum amplitude of the wave, b is the proportion of sawtooth harmonics to the pure sinusoid. The results in Fig. 3.6b shows that the sawtooth comprises a larger portion of the total wave amplitude when the driving power is high relative to the wave frequency.

3.6 Goal Summary

Thus far, the PIC simulation program has been parallelized and a number of numerical calculation tools based on linear theories have been implemented [10, 11]. The dimension space has been investigated for the following parameters.

- a : The particle dynamics was varied between linear and full electromagnetic.
- E : Changes in the electric field were sampled, especially in the previously uninvestigated low amplitude regime where $E_{skin} < 1$ V/m.
- m_i : The ion mass was varied between ∞ (immobile ions), 74400 (argon mass), and 1837 (hydrogen mass). Altering the ion mass affected the simulation results little. A future goal could be to determine when equilibrium is reached for each value.
- ω : The driving frequency was sampled between 0.25 Mhz and 128Mhz. No previous tests had been performed below 1 MHz, because the the computation time required was prohibitive.
- T : Temperature variation has been investigated slightly, although there is comparatively little data from values other than 10 eV.
- ν : Electron-neutral collisions are untested.

I wish to answer three outstanding questions during the remaining time:

1. I must find the temperature dependence of α , the PMF-to-electric field exponentiation value.
2. I must complete and test the implementation of particle collisions in the PIC code, and explore their effect on the surface impedance. No physical ICP device is collisionless. Therefore, optimization of the rf frequency must be performed with Monte-Carlo collisions enabled.
3. I must test and utilize two more programs for numerical calculation of linear results [9, 16]. This is important to verify the answers provided by the other programs, and finally, the PIC simulation.

Acknowledgements

Thanks go to Andrei Smolyakov and Dmytro Sydorenko for guidance. The computing power was supplied by Westgrid and the research funding came from the University of Saskatchewan.

BIBLIOGRAPHY

- [1] Birdsall C K, Langdon A B *Plasma Physics via Computer Simulation* Institute of Physics Publishing: Philadelphia (2001).
- [2] Chen F F *Phys. Plasmas* **8** 3008 (2001).
- [3] Fried B D, Conte S D *The Plasma Dispersion Function* Academic Publishing: New York (1961).
- [4] Godyak V *Plasma Phys. Control. Fusion* **45** A399 (2003).
- [5] Joyce G, Lampe M, Slinker S, Manheimer W *J. of Comp. Physics* **138** 540 (1997).
- [6] Karp A H, Flatt H P *Comm. of the ACM* **33** 539 (1990).
- [7] Kolobov V I, Economou D J *Plasma Sources Sci. Technol.* **6** R1 (1996).
- [8] Landau, Lifshitz *Electrodynamics of Continuous Media* Pergamon Press: New York (1984).
- [9] Shaing K C, *Phys. Plasmas* **3** 3303 (1996).
- [10] Shaing K C, Aydemir A Y *Phys. Plasmas* **4** 3163 (1997).
- [11] Smolyakov A I, Godyak V, Tyshetskiy Y *Phys. of Plasmas* **8** 3857 (2001).
- [12] Sydorenko D *Ph.D. Thesis, University of Saskatchewan* (2006).
- [13] Turner M M *Phys. Rev. Lett.* **71** 1844 (1993).
- [14] Vahedi V, Surendra M *Computer Phys. Comm.* **87** 179 (1995).
- [15] Weibel E S *Phys. Fluids* **16** 949 (1967).
- [16] Yoon N S, Kim S S, Chang C S, Choi D *Phys. Rev. E* **54** 757 (1996).